

THE EMERGENCE OF A TWISTED FLUX TUBE INTO THE SOLAR ATMOSPHERE: SUNSPOT ROTATIONS AND THE FORMATION OF A CORONAL FLUX ROPE

Y. FAN

HAO, ESSL, National Center for Atmospheric Research¹, P.O. Box 3000, Boulder, CO 80307, USA
Received 2009 January 8; accepted 2009 March 12; published 2009 May 13

ABSTRACT

We present a three-dimensional simulation of the dynamic emergence of a twisted magnetic flux tube from the top layer of the solar convection zone into the solar atmosphere and corona. It is found that after a brief initial stage of flux emergence during which the two polarities of the bipolar region become separated and the tubes intersecting the photosphere become vertical, significant rotational motion sets in within each polarity. The rotational motions of the two polarities are found to twist up the inner field lines of the emerged fields such that they change their orientation into an inverse configuration (i.e., pointing from the negative polarity to the positive polarity over the neutral line). As a result, a flux rope with sigmoid-shaped, dipped core fields forms in the corona, and the center of the flux rope rises in the corona with increasing velocity as the twisting of the flux rope footpoints continues. The rotational motion in the two polarities is a result of propagation of nonlinear torsional Alfvén waves along the flux tube, which transports significant twist from the tube’s interior portion toward its expanded coronal portion. This is a basic process whereby twisted flux ropes are developed in the corona with increasing twist and magnetic energy, leading up to solar eruptions.

Key words: Sun: activity – Sun: coronal mass ejections – Sun: flares – Sun: magnetic fields – sunspots

Online-only material: gif animation

1. INTRODUCTION

How twisted magnetic fields emerge from the dense, convectively unstable solar convection zone into the stably stratified, rarefied solar atmosphere and corona is a fundamentally important question for understanding the formation of solar active regions and the development of precursor structures for solar eruptions such as flares and coronal mass ejections (CMEs). Pioneered by the earlier work of Shibata and collaborators (Shibata et al. 1989), a large body of three-dimensional magnetohydrodynamics (MHD) simulations of the emergence of twisted magnetic flux tubes into the solar atmosphere (e.g., Fan 2001; Magara & Longcope 2001, 2003; Magara 2004, 2006; Manchester et al. 2004; Archontis et al. 2004; Murray et al. 2006; Archontis & Toëroëk 2008) has been carried out in recent years, which has provided important insight into the above dynamic process. It has been shown that magnetic flux reaching the photosphere can undergo a dynamic expansion into the atmosphere as a result of the nonlinear growth of the magnetic buoyancy instability. The conditions required of the emergent tubes for the onset of such dynamic expansion into the atmosphere have been examined by Archontis et al. (2004) and Murray et al. (2006).

These simulations have also shown that it is difficult for a twisted flux tube to rise bodily into the corona as a whole due to the heavy plasma that is trapped at the bottom concave (or U-shaped) portions of the winding field lines (e.g., Fan 2001; Manchester et al. 2004; Archontis et al. 2004; Magara 2006). While the upper parts of the helical field lines of the twisted flux tube expand into the atmosphere and the corona, the U-shaped parts of the winding field lines remain largely trapped at and below the photosphere layer, and the center of the original tube axis ceases to rise a couple of pressure scale heights above the photosphere. Despite this, a twisted

coronal flux rope with sigmoid-shaped concave upturning field lines threading under a central axis that rises into coronal heights is found to develop in the end in many simulations (e.g., Magara & Longcope 2001, 2003; Magara 2004, 2006; Manchester et al. 2004; Archontis & Toëroëk 2008). Manchester et al. (2004) found that shear flows on the photosphere driven by the magnetic tension force continually transport axial flux and magnetic energy to the upper expanded portion of the emerged field, causing it to eventually “pinch off” from the lower mass-laden part via magnetic reconnection in a current sheet forming in the lower atmosphere. This reconnection produces a coronal flux rope with a new central axial field line that rises into the corona with increasing speed. Such development of a coronal flux rope is found to take place more readily with a more sharply arched subsurface tube for which the emerging segment breaking through the photosphere contains fewer turns of field-line twist. Magara & Longcope (2003) show that during the emergence of a twisted flux tube, both the vertical emergence of magnetic flux and the horizontal motions at the footpoints of the emerged field lines inject magnetic energy and helicity (or twist) into the atmosphere. The contribution by the direct emergence dominates at the early phase of flux emergence, while the horizontal flows become a dominant contributor of helicity injection later. Magara (2006) studied in more detail the horizontal flows on the photosphere during flux emergence and found that as soon as the flux tubes intersecting the photosphere become vertical and the two polarity flux concentrations on the photosphere become separated, a rotational flow appears in each of the polarity flux concentrations.

In the present paper, we further study the role of the shear flows and the rotational flows in driving the formation of a coronal flux rope during flux emergence. We present a simulation of the emergence of a twisted Ω -shaped subsurface flux tube whose emerging segment initially breaking through the photosphere contains less than one full wind of field-line

¹ The National Center for Atmospheric Research is sponsored by the National Science Foundation.

twist. As in the simulation of Magara (2006), we find a brief initial phase of flux emergence during which the two polarity flux concentrations on the photosphere undergo a shearing motion along the neutral line and become separated. Then a prominent rotational/vortical motion develops within each polarity, reminiscent of sunspot rotations that have been observed occasionally (e.g., Brown et al. 2003). The rotational motions of the two polarities are due to torsional Alfvén waves propagating along the twisted flux tube, transporting magnetic twist from the tube’s interior portion, where the rate of twist is high, to its greatly stretched coronal portion, where the rate of twist is low, a result that was predicted by an earlier idealized analytical model of Longcope & Welsch (2000). The rotational motions of the two polarities are found to persist throughout the later phase of the evolution and steadily inject magnetic helicity into the atmosphere. The combined effect of the initial shear flow and the subsequent rotational motions of the two polarities is to twist up the inner field lines of the emerged field, causing them to rotate from their initial normal configuration (i.e., arching over the polarity inversion line from the positive to the negative polarity), into an inverse configuration (directed from the negative polarity to the positive polarity over the neutral line). In this manner, a flux rope with sigmoid-shaped dipped core fields forms in the atmosphere, with the center of the flux rope, as represented by the O-point of the transverse field in the central cross section, rising into coronal heights. This field reconfiguration is a major new finding of our study, namely that the horizontal rotation of the field direction of the lower emerged flux into an inverse configuration causes an upward propagation of the O-point, and initiates the development of the coronal flux rope. Similar to many previous simulations (e.g., Magara & Longcope 2003; Magara 2004, 2006; Manchester et al. 2004), a current sheet forms in the lower atmosphere, and the field lines whose lower parts going through the current sheet all display a sigmoid morphology, which may correspond to the observed X-ray sigmoid loops in active regions.

The remainder of the paper is structured as follows. In Section 2, we describe the numerical MHD model and the detailed setup of the simulation. In Section 3, we describe the simulation results, with focus on examining the nature of the rotational motion of the two polarities on the photosphere and how it drives the formation of a flux rope in the corona. Finally, in Section 4 we summarize the conclusions and discuss the implications of our simulation results.

2. THE NUMERICAL MODEL

In this study, we solve numerically the following ideal MHD equations in a Cartesian domain:

$$\frac{\partial \rho}{\partial t} + \nabla \cdot (\rho \mathbf{v}) = 0, \quad (1)$$

$$\frac{\partial(\rho \mathbf{v})}{\partial t} + \nabla \cdot (\rho \mathbf{v} \mathbf{v}) = -\nabla p + \rho \mathbf{g} + \frac{1}{4\pi} (\nabla \times \mathbf{B}) \times \mathbf{B} \quad (2)$$

$$\frac{\partial \mathbf{B}}{\partial t} = \nabla \times (\mathbf{v} \times \mathbf{B}), \quad (3)$$

$$\nabla \cdot \mathbf{B} = 0, \quad (4)$$

$$\frac{\partial e}{\partial t} = -\nabla \cdot \left[\left(\varepsilon + \frac{\rho v^2}{2} + p \right) \mathbf{v} - \frac{1}{4\pi} (\mathbf{v} \times \mathbf{B}) \times \mathbf{B} \right] + \rho \mathbf{v} \cdot \mathbf{g}, \quad (5)$$

$$p = \frac{\rho RT}{\mu}, \quad (6)$$

where

$$e = \varepsilon + \frac{\rho v^2}{2} + \frac{B^2}{8\pi}, \quad (7)$$

$$\varepsilon = \frac{p}{\gamma - 1}. \quad (8)$$

In the above \mathbf{v} , \mathbf{B} , ρ , p , T , R , μ , ε , e denote, respectively, the velocity field, the magnetic field, density, pressure, temperature, the gas constant, the mean molecular weight, the internal energy per unit volume, and the total energy (internal+kinetic+magnetic) per unit volume. The gravitational acceleration $\mathbf{g} = -g\hat{\mathbf{z}}$ is a constant and is directed in the $-z$ direction. The above ideal MHD equations are solved numerically without any *explicit* viscosity, magnetic diffusion, and nonadiabatic effects, although numerical dissipations are present. Thus we do not physically treat the radiative energy transfer, thermal conduction, coronal heating, and the effects of partial ionization, which all play important roles in the thermal energy evolution of the plasma in the solar atmosphere. The thermal properties of the plasma in our simulations are therefore unrealistic. Our study here focuses on the dynamic and topological properties of the three-dimensional emerging magnetic field, given the above simplifications.

The basic numerical schemes we use to solve the above MHD equations are as follows. The equations are discretized in space using a staggered finite-difference scheme (Stone & Norman 1992a), and advanced in time with an explicit, second-order accurate, two-step predictor–corrector time stepping. A modified, second-order accurate Lax–Friedrichs scheme similar to that described in Rempel et al. (2009, see Equation (A3) in that paper) is applied for evaluating the fluxes in the continuity, momentum, and energy equations. Compared to the standard second-order Lax–Friedrichs scheme, this scheme significantly reduces numerical diffusivity for regions of smooth variation, while retaining the same robustness in regions of shocks. A method of characteristics that is upwind in the Alfvén waves (Stone & Norman 1992b) is used for evaluating the $\mathbf{v} \times \mathbf{B}$ term in the induction equation, and the constrained transport scheme is used to ensure $\nabla \cdot \mathbf{B} = 0$ to machine round-off errors.

The equations are nondimensionalized using the following normalizing constants: $\rho_{\text{ph}} \approx 2.7 \times 10^{-7} \text{ g cm}^{-3}$ (photospheric density), $H_{\text{ph}} \approx 150 \text{ km}$ (pressure scale height at the photosphere), $T_{\text{ph}} \approx 5100 \text{ K}$ (photospheric temperature), $v_{\text{th}} = (\mathcal{R}T_{\text{ph}}/\mu)^{1/2} \approx 6.5 \text{ km s}^{-1}$ (isothermal sound speed at the photosphere), $t_{\text{ph}} = H_{\text{ph}}/v_{\text{th}} \approx 23 \text{ s}$, $p_{\text{ph}} = \rho_{\text{ph}} v_{\text{th}}^2$ (photospheric pressure), and $B_{\text{ph}} = (4\pi \rho_{\text{ph}} v_{\text{th}}^2)^{1/2} \approx 1200 \text{ G}$, as the units for density, length, temperature, velocity, time, pressure, and magnetic field, respectively. For the remainder of the paper, quantities and equations are expressed in the above units unless otherwise specified.

The setup of the numerical simulation is illustrated in Figure 1. The simulation domain (the top panel of Figure 1) is $(-69.3, -63.6, -20) \leq (x, y, z) \leq (69.3, 63.6, 115)$, resolved by a $320 \times 300 \times 392$ grid. In the x -direction (y -direction), the mesh size is $\Delta x = 0.2$ ($\Delta y = 0.2$) within $-20 \leq x \leq 20$ ($-20 \leq y \leq 20$), and it increases gradually for $|x| > 20$ ($|y| > 20$), reaching about 2 at the boundaries. In the z -direction, the mesh size is $\Delta z = 0.2$ within the range $-20 \leq z \leq 32$, and for $z > 32$ it increases gradually to 1.39 at the top boundary. The horizontal boundaries in the x -direction (the direction of the

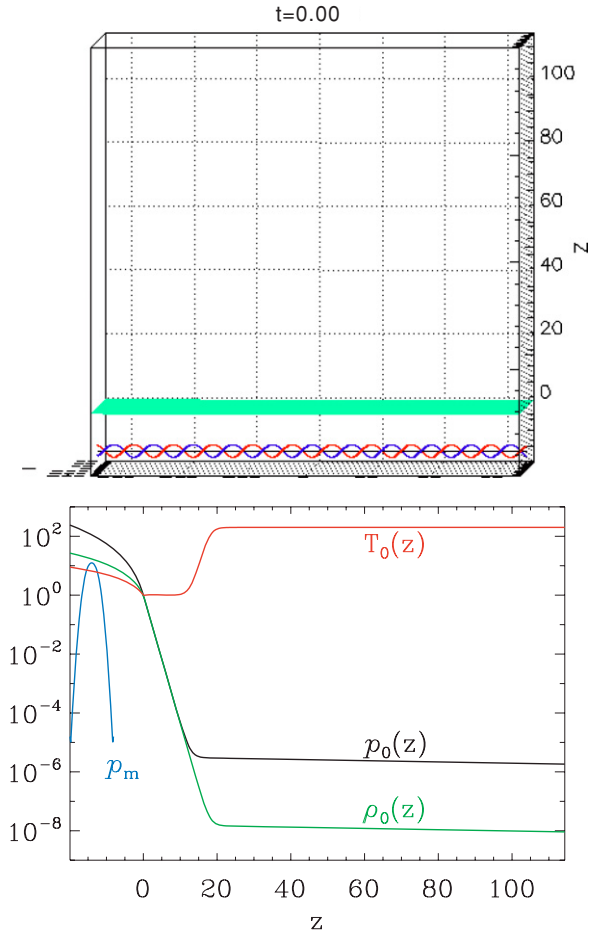


Figure 1. Initial setup of the simulation. The top panel shows the simulation domain, where the green plane denotes the photosphere and the configuration of the initial flux tube is illustrated with three traced field lines in the flux tube. The bottom panel shows the vertical profiles of plasma pressure, density, and temperature of the field-free static atmosphere, and also the profile of the magnetic pressure through the embedded flux tube along the center line at $(x, y) = (0, 0)$.

initial flux tube) are assumed to be periodic. The bottom boundary is a perfectly conducting wall and is nonpenetrating. An outflow boundary condition (see Stone & Norman 1992a) is applied for the top boundary and the two horizontal boundaries in the y -direction. For the initial state, we consider a plane-parallel atmosphere in hydrostatic equilibrium, composed of an adiabatically stratified polytropic layer representing the top layer of the convection zone, an isothermal layer representing the photosphere and the chromosphere, connecting to another isothermal layer of 1 MK representing the corona. The vertical profiles of the pressure $p_0(z)$, density $\rho_0(z)$, and temperature $T_0(z)$ of the hydrostatic field-free atmosphere are shown in the bottom panel of Figure 1. A horizontal, twisted magnetic flux tube oriented along the x -direction is embedded in the polytropic layer (convection zone) with its axis located at $(y, z) = (0, -14)$. The magnetic field of the flux tube is given by

$$\mathbf{B} = B_x(r) \hat{\mathbf{x}} + B_\theta(r) \hat{\theta}, \quad (9)$$

where

$$B_x(r) = B_0 \exp(-r^2/a^2), \quad (10)$$

$$B_\theta(r) = qr B_x(r). \quad (11)$$

In the above $\hat{\mathbf{x}}$ is the tube axial direction, $\hat{\theta}$ is the azimuthal direction in the tube cross section, and r denotes the radial distance to the tube axis. The flux tube is uniformly twisted, with the constant q denoting the angle of field-line rotation about the axis over a unit length of the tube. We set $B_0 = 5$, the radius $a = 2$, and the rate of twist $q = -a^{-1}$ (left-handed), which makes the tube marginally stable for the kink instability (Linton et al. 1996). The profile of the magnetic pressure p_m along the vertical line at $(x, y) = (0, 0)$ through the center of the embedded tube is also shown in Figure 1. Inside the flux tube, the plasma pressure differs from that of the hydrostatic field-free atmosphere $p_0(z)$ by

$$p_1(r) = -\frac{B_0^2}{2} \exp(-2r^2/a^2) \left[1 - \frac{1}{2} q^2 a^2 \left(1 - \frac{2r^2}{a^2} \right) \right], \quad (12)$$

satisfying the equation

$$\frac{dp_1}{dr} = -\frac{d}{dr} \left(\frac{B_x^2 + B_\theta^2}{2} \right) - \frac{B_\theta^2}{r}. \quad (13)$$

which ensures that the pressure gradient in the flux tube balances the Lorentz force. To make the flux tube buoyant, we further impose a density change ρ_1 within the flux tube relative to $\rho_0(z)$ of the field-free hydrostatic atmosphere:

$$\rho_1 = -\rho_0(z) \frac{B_x^2(r)}{2p_0(z)} [(1 + \epsilon) \exp(-x^2/\lambda^2) - \epsilon], \quad (14)$$

where $\lambda = 8$ and $\epsilon = 0.2$. This makes the middle portion of the flux tube buoyant, with $\rho_1/\rho_0 = -0.11$ at the middle of the tube axis. The buoyancy declines with $|x|$ from $x = 0$ following a Gaussian profile with an e -folding length of λ , and the two ends are slightly antibuoyant with $\rho_1/\rho_0 = 0.022$ at the ends of the tube axis. The plasma β (defined as the ratio of the plasma pressure over the magnetic pressure) is about 8.3 at the axis of the tube.

3. RESULTS

3.1. Overview of the Evolution

The early evolution of the buoyant flux tube is qualitatively similar to those reported in many previous investigations (e.g., Magara & Longcope 2001; Fan 2001; Magara 2004, 2006; Manchester et al. 2004; Archontis et al. 2004; Murray et al. 2006). The central portion of the initial flux tube rises buoyantly while the two ends of the flux tube sink down toward the bottom owing to the slight negative buoyancy there. The flux tube develops into an Ω -shape, whose central apex portion rises toward the photosphere. When the flux tube enters the stably stratified photosphere, magnetic pressure builds up at the photosphere layer and the magnetic buoyancy instability develops. This causes a rapid expansion of the front of the flux tube into the solar atmosphere and initiates the flux emergence.

Figures 2 and 3 show, respectively, two perspective views of the three-dimensional magnetic field as delineated by a set of representative field lines at four time instances during the flux emergence into the solar atmosphere. We see that at $t = 65$ the apex of the flux tube has broken through the photosphere and the front of the emerging flux tube begins to expand rapidly into the atmosphere and corona. With time, a twisted flux rope structure with field lines winding about a central axis (as represented by the black line) is formed in the atmosphere (see

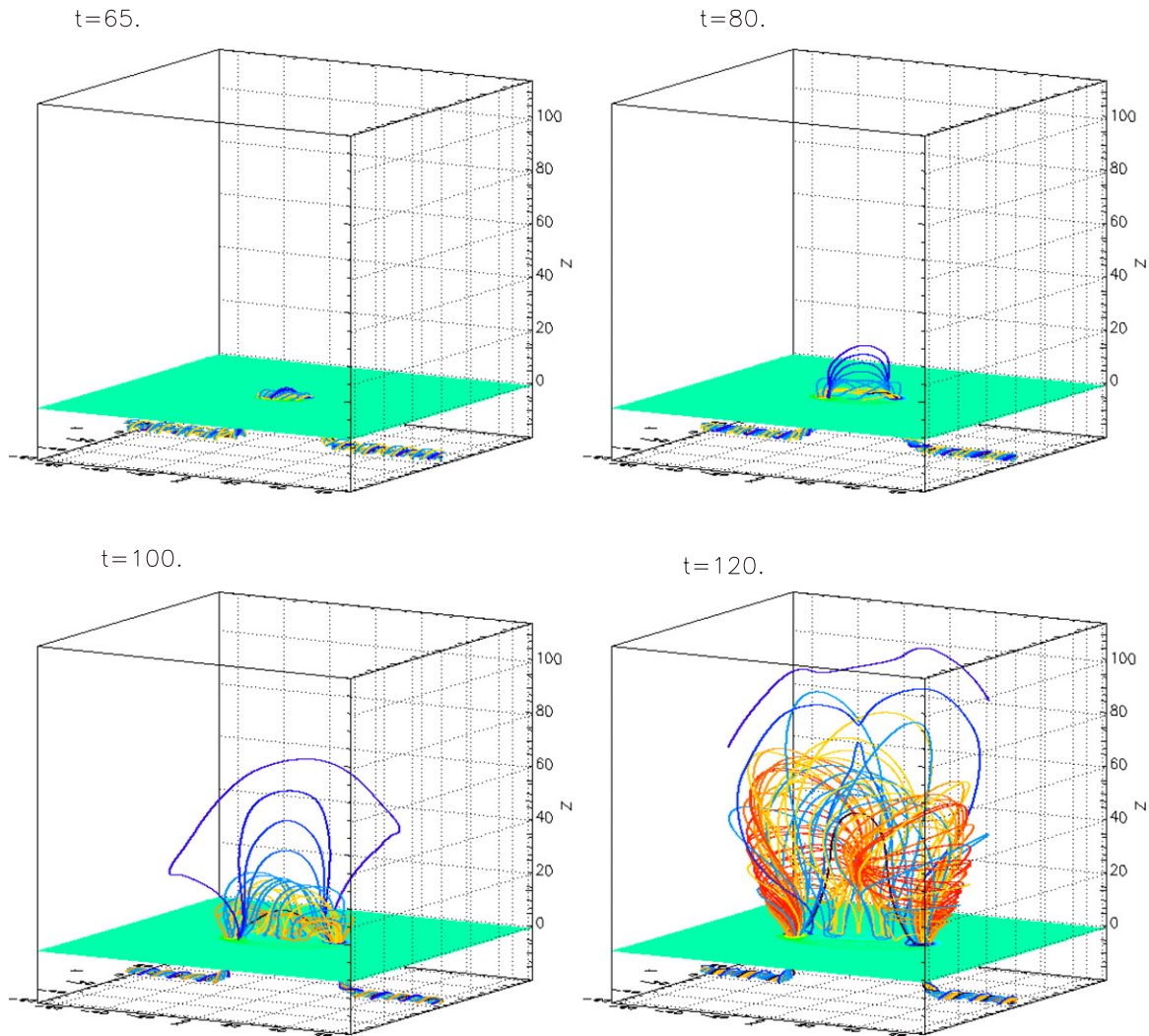


Figure 2. Snapshots of the three-dimensional magnetic field during the flux emergence into the atmosphere. Note that field lines in the different snapshots are not the same field lines carrying the same plasma—they are simply field lines selectively drawn in each instance to reflect the topological structure of the three-dimensional field. The black field line shown in each of the panels is the field line that is drawn from the O-point of the transverse field in the central cross section (at $x = 0$), and it corresponds to a different field line in each time.

the $t = 100$ and $t = 120$ panels). By time $t = 120$, the central axis of the flux rope structure has reached coronal heights, and sigmoid-shaped field lines (see the orange and red field lines), some of which containing dips, thread under the central axis with an inverse configuration (i.e., pointing from the negative to positive polarity region over the neutral line). Note that field lines in different images are not the same field lines carrying the same plasma. They are simply field lines selectively drawn in each instance to reflect the topological structure of the three-dimensional field. For example, the black axis in each panel corresponds to a *different* field line in each of the time instances, an important point to be addressed later in Section 3.2.

Figures 4(a) and (b) show the evolution of the height and rise velocity for three different points within the central vertical plane of $x = 0$: (1) the front of the emerging flux tube, (2) the Lagrangian position of the original tube axis, and (3) the O-point of the transverse magnetic field in the central vertical plane at $x = 0$, which is the point where $B_y = 0$ on the central vertical line of $x = 0$ and $y = 0$. Figure 5 shows an example snapshot of the central vertical plane of $x = 0$ at time $t = 108$, where the arrows show the direction of the transverse magnetic field in the plane, overlaid with a color image showing density on a log

scale. Note, only the part above the photosphere is shown, and the arrow lengths are all the same, normalized by the transverse field strength, for the points where the transverse field strengths are nonzero. The O-point of the transverse magnetic field is marked by the pink “*” point, and it has reached the height of the base of the corona at $t = 108$. It should be emphasized that the O-point position is based on a geometric definition which depends on the variation of B_y with z along the central vertical line of $x = 0$ and $y = 0$. Thus it does not track a Lagrangian plasma element, and its height variation with time *does not in general reflect the true vertical plasma motion* but is strongly influenced by the change with time of the horizontal magnetic field orientations at points along the central vertical line. For these reasons, dz/dt of $z(t)$ for the O-point position shown in Figure 4(a) does not in general agree with v_z , the vertical velocity of the plasma instantaneously residing at the O-point shown in Figure 4(b) (dashed line). We also note that the black field line shown in each of the panels in Figures 2 and 3 is the field line that is drawn from the O-point at that instance, and it corresponds to a different field line in each time.

From the position and the rise velocity of the front of the flux tube as shown in Figure 4, one can see that the onset of

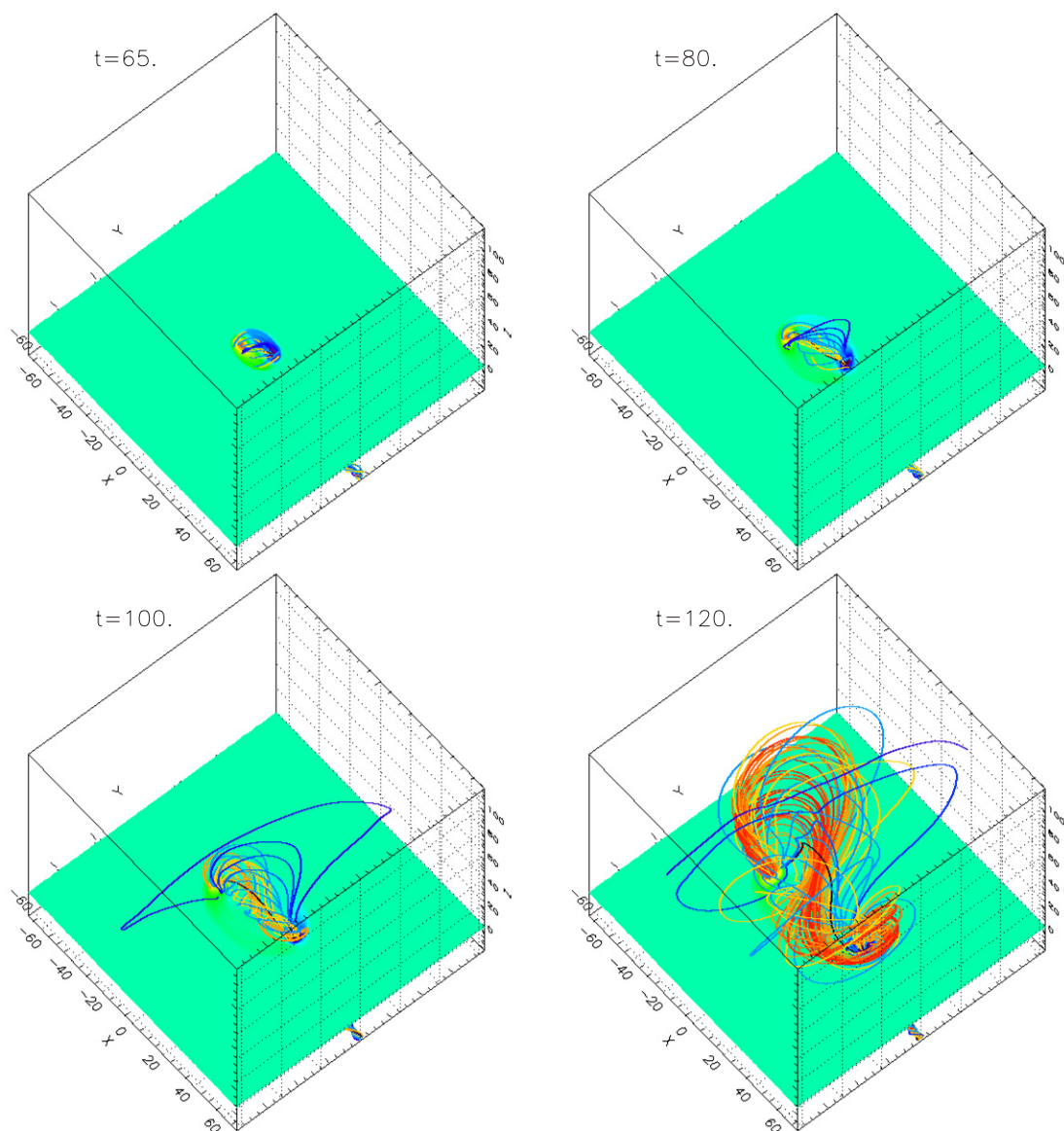


Figure 3. Same as Figure 2, but viewed from a different perspective.

the magnetic buoyancy instability and flux emergence into the atmosphere takes place at about $t = 60$, at which time there is an exponential increase of the vertical speed of the front. Archontis et al. (2004) and Murray et al. (2006) have, based on the original work of Newcomb (1961), Thomas & Nye (1975), and Acheson (1979), given the following critical condition for the onset of magnetic buoyancy instability and flux emergence at the photospheric layer:

$$-H_p \frac{\partial}{\partial z} (\log B) > -\frac{\gamma}{2} \beta \delta + k_{\parallel}^2 \left(1 + \frac{k_{\perp}^2}{k_z^2} \right), \quad (15)$$

where z is height, H_p is the local pressure scale height at the photosphere, B is the magnetic field strength, γ is the ratio of the specific heats, β is the ratio of the plasma pressure over the magnetic pressure, $\delta \equiv \nabla - \nabla_{\text{ad}}$ is the superadiabaticity of the atmosphere, which is -0.4 for the isothermal stratification of the photosphere, and k_{\parallel} , k_{\perp} , and k_z are the three components of the local perturbation wave vector (normalized by $1/H_p$), with k_{\parallel} and k_{\perp} being the two horizontal components parallel

and perpendicular to the local magnetic field direction, and k_z being the z -component. We find that at $t = 60$ the buildup of magnetic pressure at the photosphere layer has just exceeded the gas pressure, forming a layer of low plasma β (see the top panel of Figure 6), where the strong stabilizing term $-(\gamma/2)\beta\delta$ is reduced to become smaller than $-H_p(\partial/\partial z)(\log B)$ (see the bottom panel of Figure 6). Using the horizontal widths l_x and l_y of the emerging magnetic region at $z = 2$ to estimate $k_{\parallel} \sim 2\pi/l_y$ and $k_{\perp} \sim 2\pi/l_x$, and $k_z \sim 2\pi/\text{tube radius}$, we find that the above critical condition is met at $z \approx 2$.

As the front of the emerging flux tube begins to expand into the atmosphere at about $t = 60$, the rise speed of the original tube axis (the solid curve in Figure 4(b)) and the rise speed measured at the location of the O-point (the dashed curve in Figure 4(b)) both begin to decline, and their positions remain below $z = 5$ during the period from $t = 65$ to $t = 86$ (see Figure 4(a)). However, soon after $t = 86$ there is an upward jump of the O-point position, and then its height continues to increase sharply. With the O-point moving into coronal heights, a flux rope with dipped, sigmoid-shaped core field

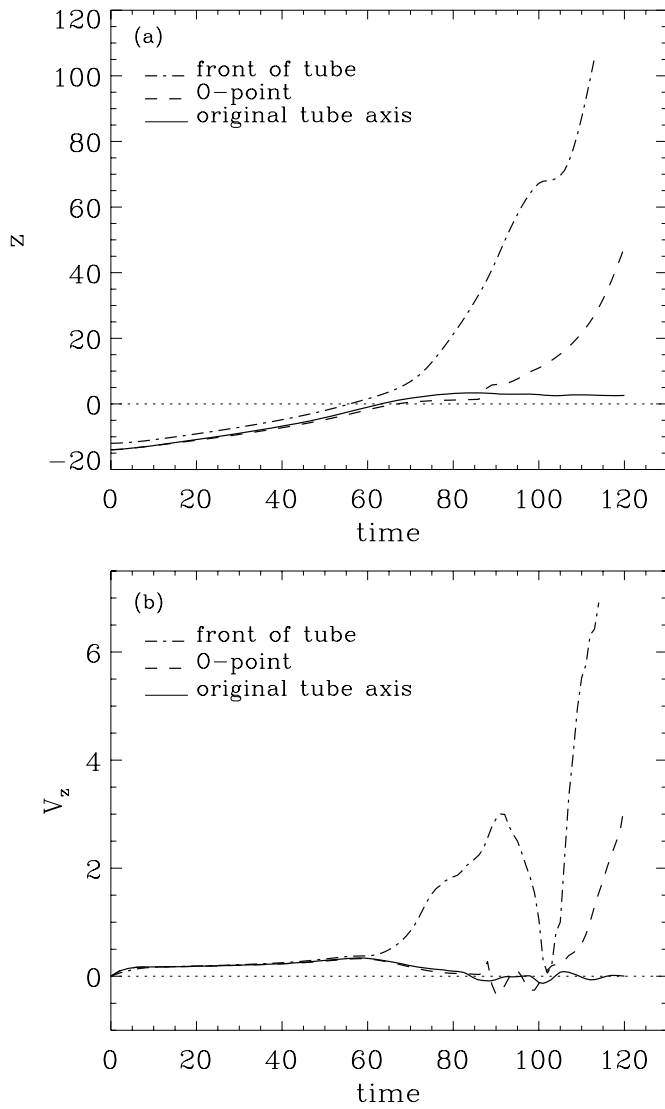


Figure 4. Evolution of the height (a) and vertical velocity (b) for three different points within the central vertical plane of $x = 0$: (1) the front of the emerging flux tube (dash-dotted line), (2) the Lagrangian position of the original tube axis (solid line), and (3) the O-point of the transverse magnetic field in the central cross section (at $x = 0$ and $y = 0$), which is the point where $B_y = 0$ on the center vertical line of $x = 0$ and $y = 0$. The midpoints of the black field lines shown in Figures 2 and 3 correspond to the O-point positions at those instances.

(see the $t = 120$ panels in Figures 2 and 3) develops in the corona.

3.2. Vortical Motion of the Two Polarities and Flux Rope Formation

To understand the apparent rise of the O-point into coronal heights and the formation of the coronal flux rope, we have tracked the evolution of a set of field lines which intersect the center vertical line of the domain (at $x = 0$ and $y = 0$). The way we do this is by tracking the motion of a few Lagrangian points situated along the center vertical line of symmetry at $x = 0$ and $y = 0$, and trace out field lines through these points at successive time instances from $t = 65$ to $t = 120$. Figures 7–9 show three-dimensional evolution of these tracked field lines as viewed from three perspectives. The black field line here corresponds to the original tube axis, and all the other field lines have their midpoints (at $x = 0$, $y = 0$) above the midpoint of the black field line (reddish field lines have midpoints above bluish field lines).

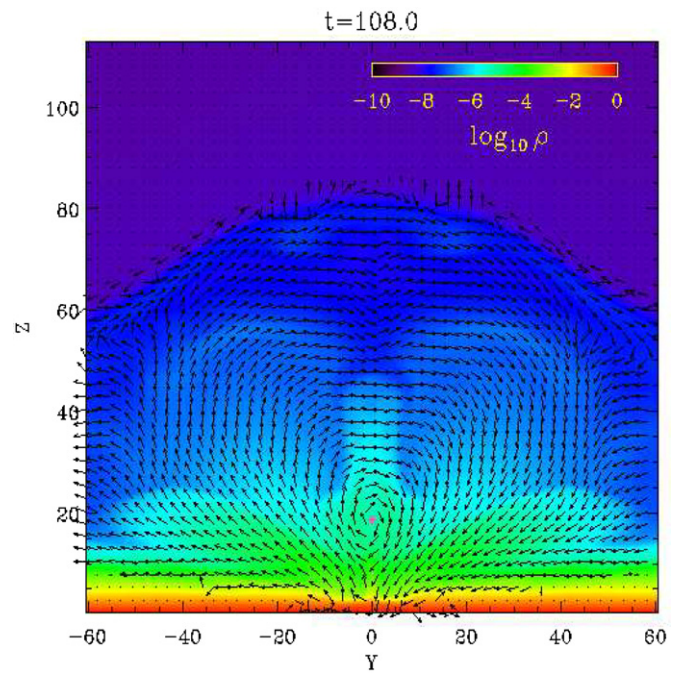


Figure 5. Snapshot of the central vertical plane of $x = 0$ at $t = 108$, with arrows showing the direction of the transverse magnetic field (lengths of the arrows are all the same, normalized by the transverse magnetic field strength for all points where the transverse field strength is nonzero), overlaid with a color image showing the density in log scale. Only the part above the photosphere is shown. The O-point of the transverse magnetic field is marked by the pink “*” point.

Note that the apex of the red field line does not correspond to the emerging front, but is significantly below it. Thus its position and rise speed do not correspond to the dash-dotted lines for the front of the emerging tube shown in Figure 4. In this sequence of images, a field line of a particular color corresponds to the same field line carrying the same plasma. A corresponding animated gif movie showing the evolution of the tracked field lines is also available in the electronic edition.

At the beginning of the flux emergence (see the $t = 65$ image in Figure 8), the field lines all show a normal configuration, i.e., they arch over the polarity inversion line from the positive to the negative polarity region. The B_y -components of these field lines at the midpoints are all positive. Thus at this time, the O-point, which is the point of zero B_y on the central vertical line, is located below the black field line (the original tube axis). With time the two polarity regions on the photosphere begin to show a significant shearing motion along the neutral line (e.g., Manchester & Low 2000; Manchester 2001; Manchester et al. 2004; Magara & Longcope 2003; Magara 2004, 2006), and the two polarity regions begin to separate. As a result the lower lying black (original axial field line) and dark blue field lines are lengthened and begin to rotate (clockwise) toward an inverse configuration, with their B_y changing from positive to negative at the midpoints (see Figure 8). By time $t = 90$ (see Figure 8), the black and dark blue field lines have rotated to show a slight negative B_y at their midpoints, while the upper yellow and red field lines are still having positive B_y at their midpoints. This change of orientations of the lower (black and dark blue) field lines from positive B_y to negative B_y causes an abrupt upward shift of the zero point of B_y along the center vertical line of $x = 0$ and $y = 0$, i.e., an upward shift of the O-point seen in Figure 4(a) (soon after $t = 85$). As a result, the O-point

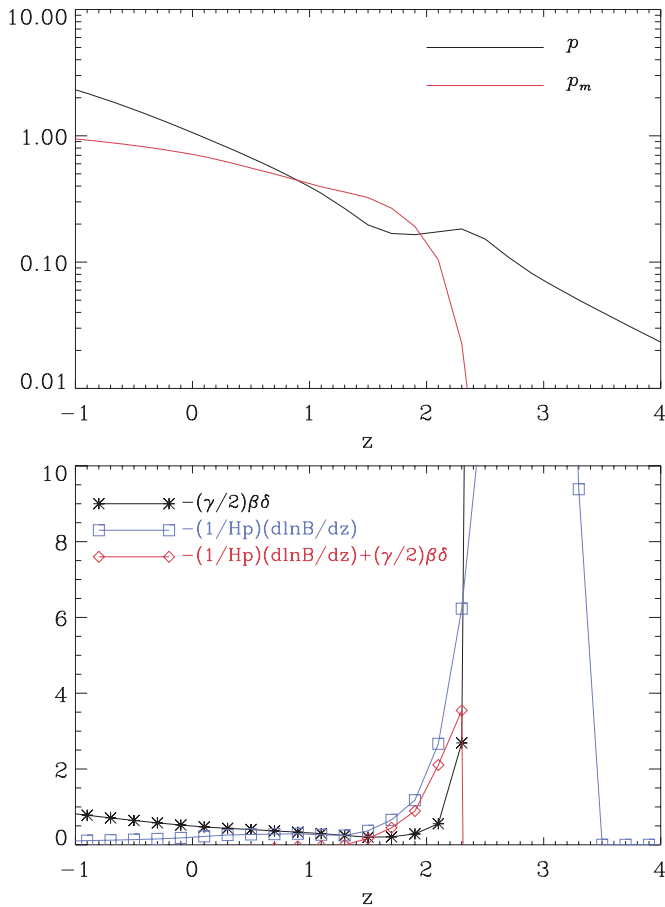


Figure 6. Vertical profiles of several quantities near the photosphere along the center line of $(x, y) = (0, 0)$, at $t = 60$. It shows the conditions of the emerging field entering the photosphere when it becomes unstable to the onset of the magnetic buoyancy instability (see discussion in the text).

position shifts from below to above the original tube axis (the black field line in Figures 7–9). This apparent crossing of the O-point position from below to above the original tube axis (as seen between $t = 85$ and $t = 90$ in Figure 4(a)) is not a true plasma rise motion, but is simply due to the change of horizontal field-line orientations in the atmosphere: the original tube axis (the black field line tracked in Figure 8) rotates from a forward into an inverse configuration, with B_y at its midpoint changing from positive to negative, and as a result the zero point of B_y on the center vertical line of $x = 0$ and $y = 0$, namely the O-point, propagates upward in position to a *different* field line above, which is now aligned with the x -direction.

By time of about $t = 90$, a significant counterclockwise vortical or rotational motion has set in within each of the two polarity flux concentrations on the photosphere, reminiscent of sunspot rotations (e.g., Brown et al. 2003). The vortical motions can be seen from the footpoint motions of the field lines in Figures 7–9 (and in the movie), and more clearly in Figure 10 which shows snapshots of the z -component of the vorticity ω_z on the photosphere overlaid with contours of B_z . We find high intensity of positive ω_z (corresponding to counterclockwise vortical motion) centered on the peaks of the vertical magnetic flux concentration of both polarities. Figure 11 shows the evolution of the mean vertical vorticity $\langle \omega_z \rangle$ averaged over the area of each polarity flux concentration where B_z is above 75% of the peak B_z value. We find that the

counterclockwise vortical motion centered on each polarity flux concentration, as represented by $\langle \omega_z \rangle$, rises to its peak rate at $t \approx 93$ and then persists at a relatively steady rate throughout the subsequent evolution. The footpoint vortical motions further twist up the emerged field lines, causing continued clockwise horizontal rotation of the blue and the higher yellow and red field lines in the atmosphere as viewed from the top (see the $t = 100$, $t = 110$, $t = 118$, and $t = 120$ panels in Figure 8, and the movie associated with Figure 7). With time, the yellow and then red field lines are also progressively rotated into an inverse configuration, changing the sign of B_y from positive to negative at their midpoints. This causes the O-point position (the zero B_y position on the center line of $x = 0$, $y = 0$) to continue to propagate upward as seen in Figure 4(a) after about $t = 90$. Note again that this upward shift of the O-point position from $t = 86$ to about $t = 102$ is not due to a true vertical rise of the plasma as can be seen from the near zero v_z during this period shown in Figure 4(b), but is simply a propagation effect produced by the change of horizontal orientations of the emerged field lines.

Starting from about $t = 102$, the plasma rise velocity v_z measured at the O-point position also shows a significant upward acceleration (see Figure 4(b)), which means that the rapid ascent of the O-point after about $t = 102$ (see Figure 4(a)) is a combination of the upward propagation produced by the change of the horizontal orientations of the field lines and an actual rise motion of the field lines. At about $t = 118$ (see Figure 8), the O-point position has reached $z = 40.2$, which is at this instant identified with the midpoint of the red field line. The red field line has rotated to become aligned with the x -direction with zero B_y at the middle and is at this instant identified as the axial field line of the coronal flux rope. The plasma rise speed v_z measured at the O-point is about 2.6 (or 16.9 km s⁻¹), which continues to increase (see Figure 4(b)). The field lines continue to rotate horizontally. As a result, the field line identified as the coronal axial field line is continually changing. By time $t = 120$, the red field line has further rotated to having a negative B_y at its center, and the O-point has now shifted to a field line (not shown in Figures 7–9) above the red field line.

We also find that in conjunction with the horizontal rotation of the black and blue field lines in the atmosphere due to shearing and twisting at their footpoints, they develop central dips, into which plasma drains, and the two-side “wings” of each of these field lines rise rapidly into the corona (see the $t = 100$, $t = 110$, $t = 118$, $t = 120$ images in Figures 7 and 9).

The above examination of the tracked field lines indicates that the formation and rise of the coronal flux rope is not a result of the bodily emergence of the subsurface flux tube as a whole. The bottom concave portions of the helical field lines in the original emerging flux tube breaking through the surface remain largely trapped at and below the photosphere layer due to the weight of the heavy plasma, and the center of the original tube axis ceases to rise after reaching about 2–3 pressure scale heights above the photosphere. However, the shearing and vortical motions of the two polarity flux concentrations at the photosphere continue to transport twist and magnetic energy into the emerged field in the atmosphere (e.g., Magara & Longcope 2003; Manchester et al. 2004; Magara 2006). Our analysis in this paper shows that due to this vortical motion at the footpoints, the emerged field lines near and just above the original axial field line (including the original axial field line itself) rotate horizontally in the atmosphere, changing B_y at their midpoints from positive to negative (i.e., from an original normal configuration to an

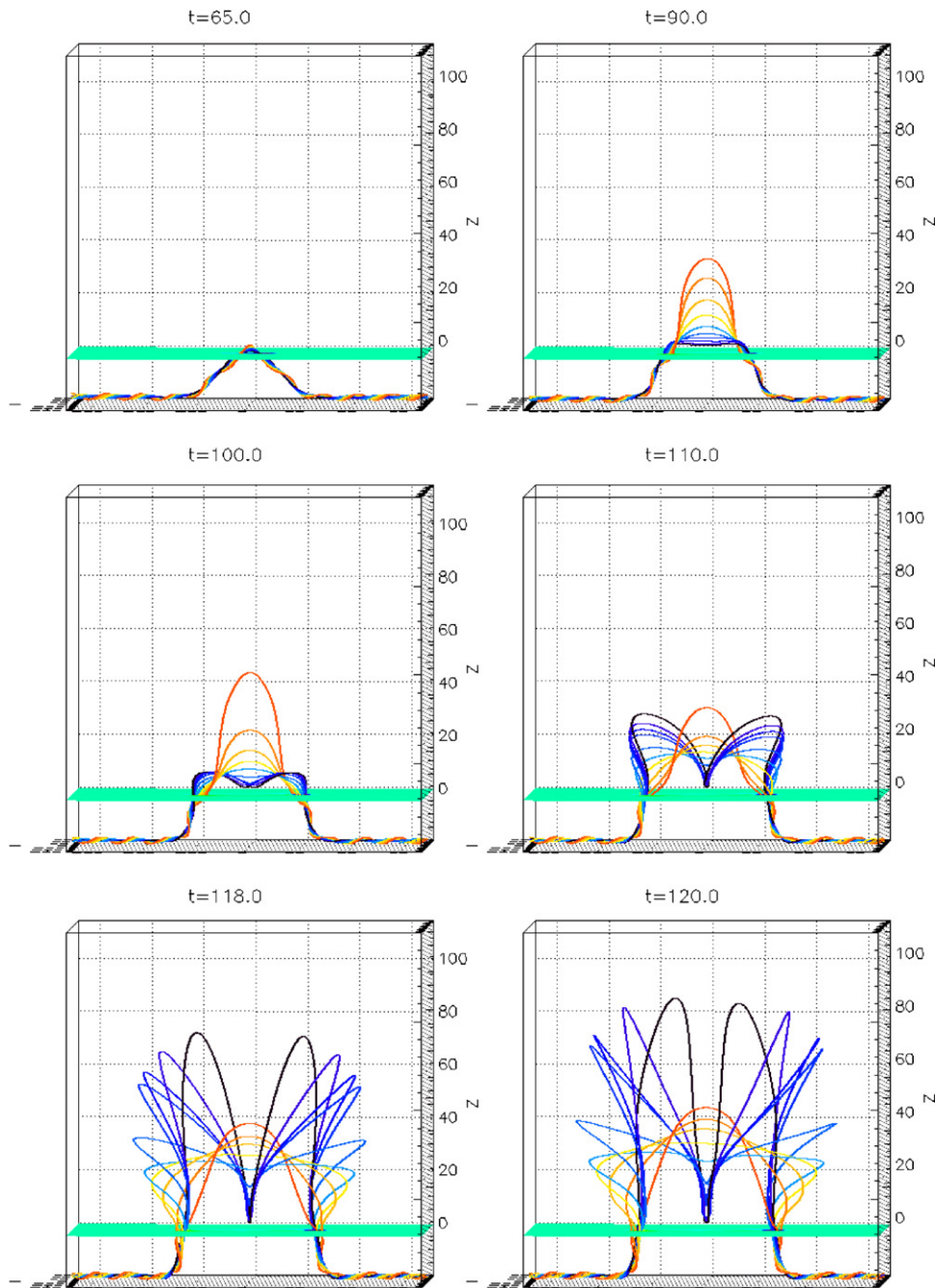


Figure 7. Three-dimensional evolution of a set of tracked field lines as they are being twisted up by the shear and rotation motions at their footpoints on the photosphere. In this sequence of images, a field line of a particular color corresponds to the same field line carrying the same plasma. The black field line corresponds to the original tube axis, and all the other field lines have their midpoints (at $x = 0$, $y = 0$) above the midpoint of the black field line (reddish field lines have midpoints above bluish field lines).

(A gif animation of this figure is available in the online journal.)

inverse configuration with respect to the photosphere neutral line). This initiates an upward *propagation* of the O-point in the emerged field in the central $x = 0$ cross section simply because of the change of horizontal orientation of the inner field lines, and not because of the rise of these field lines. Later, the plasma rise speed measured at the O-point also shows a sharp increase, contributing to the rapid ascent of the O-point into coronal heights. As a result, a coronal flux rope with an axis identified with the field line instantaneously aligned with the x -direction at its midpoint (i.e., going through the O-point) and with sigmoid-shaped field lines threading under the axis with an

inverse configuration develops, and it is rising with increasing velocity as the vortical motions at the footpoints of the flux rope continue to transport magnetic energy and twist into the corona. Note that the field line being identified as the axial field line of the coronal flux rope is continually changing, due to the continued horizontal rotation of the field lines in the atmosphere as their footpoints are being twisted.

To quantify the transport of twist into the solar atmosphere due to both flux emergence as well as the horizontal vortical motions at the photosphere, we have computed the evolution of the relative magnetic helicity in the atmosphere above the

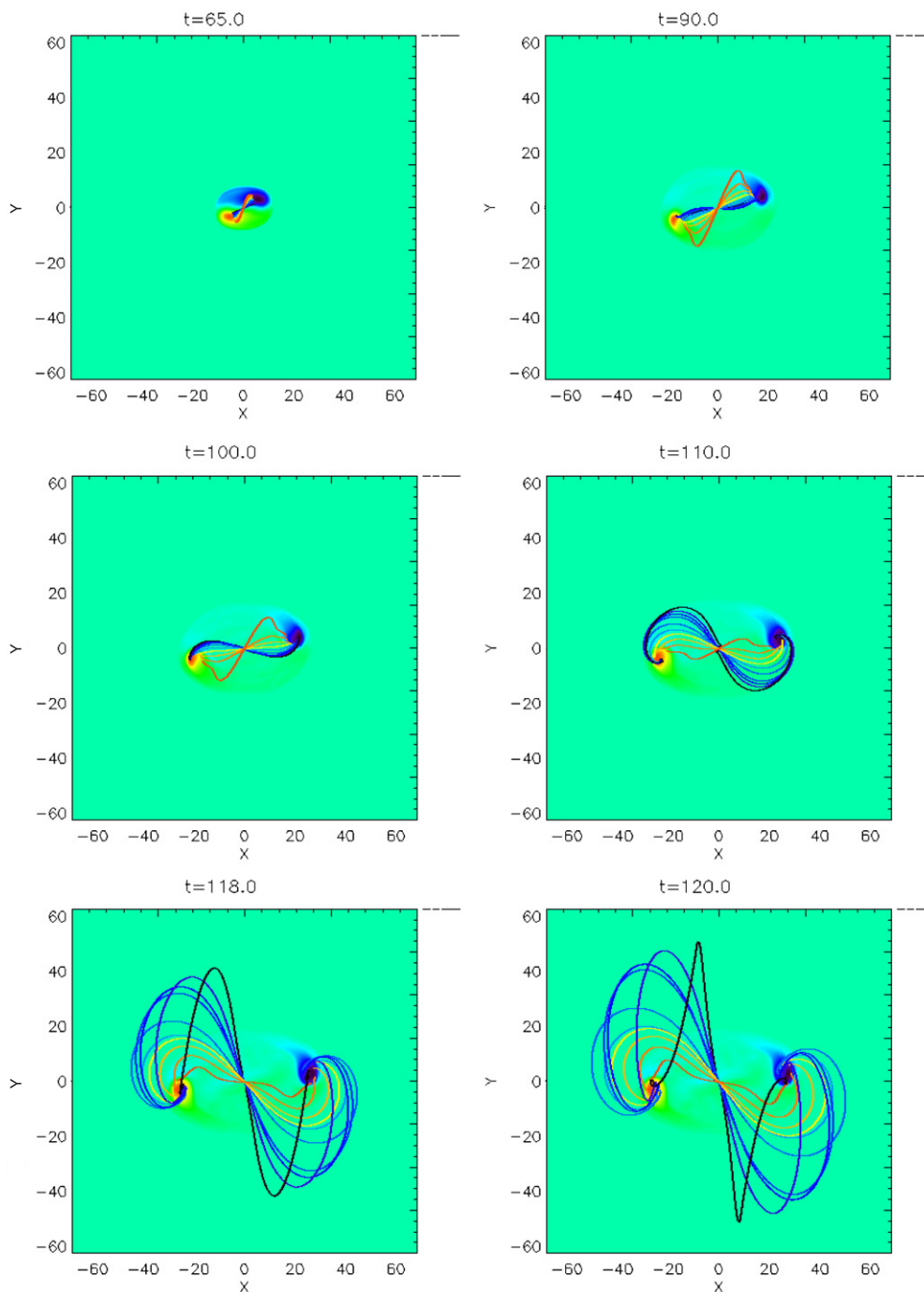


Figure 8. Same as Figure 7, but is viewed from the top.

photosphere and the helicity flux through the photospheric boundary. The relative magnetic helicity in the atmosphere above the photosphere $z = 0$ is defined as (Berger & Field 1984; Finn & Antonsen 1985)

$$H_m = \int_{z>0} (\mathbf{A} + \mathbf{A}_p) \cdot (\mathbf{B} - \mathbf{P}) dV, \quad (16)$$

where \mathbf{B} is the magnetic field in the unbounded half space above $z = 0$, \mathbf{A} is the vector potential for \mathbf{B} , \mathbf{P} is the reference potential field having the same normal flux distribution as \mathbf{B} on the $z = 0$ boundary, and \mathbf{A}_p is the vector potential for \mathbf{P} . The relative magnetic helicity H_m is invariant with respect to the gauges for \mathbf{A} and \mathbf{A}_p . Following Devore (2000), we use the following

specific \mathbf{A} and \mathbf{A}_p for computing H_m :

$$\mathbf{A}(x, y, z) = \mathbf{A}_p(x, y, 0) - \hat{\mathbf{z}} \times \int_0^z \mathbf{B}(x, y, z') dz', \quad (17)$$

$$\mathbf{A}_p(x, y, z) = \nabla \times \hat{\mathbf{z}} \int_z^\infty \phi(x, y, z') dz', \quad (18)$$

where

$$\phi(x, y, z) = \frac{1}{2\pi} \iint \frac{B_z(x', y', 0)}{[(x - x')^2 + (y - y')^2 + z^2]^{1/2}} dx' dy'. \quad (19)$$

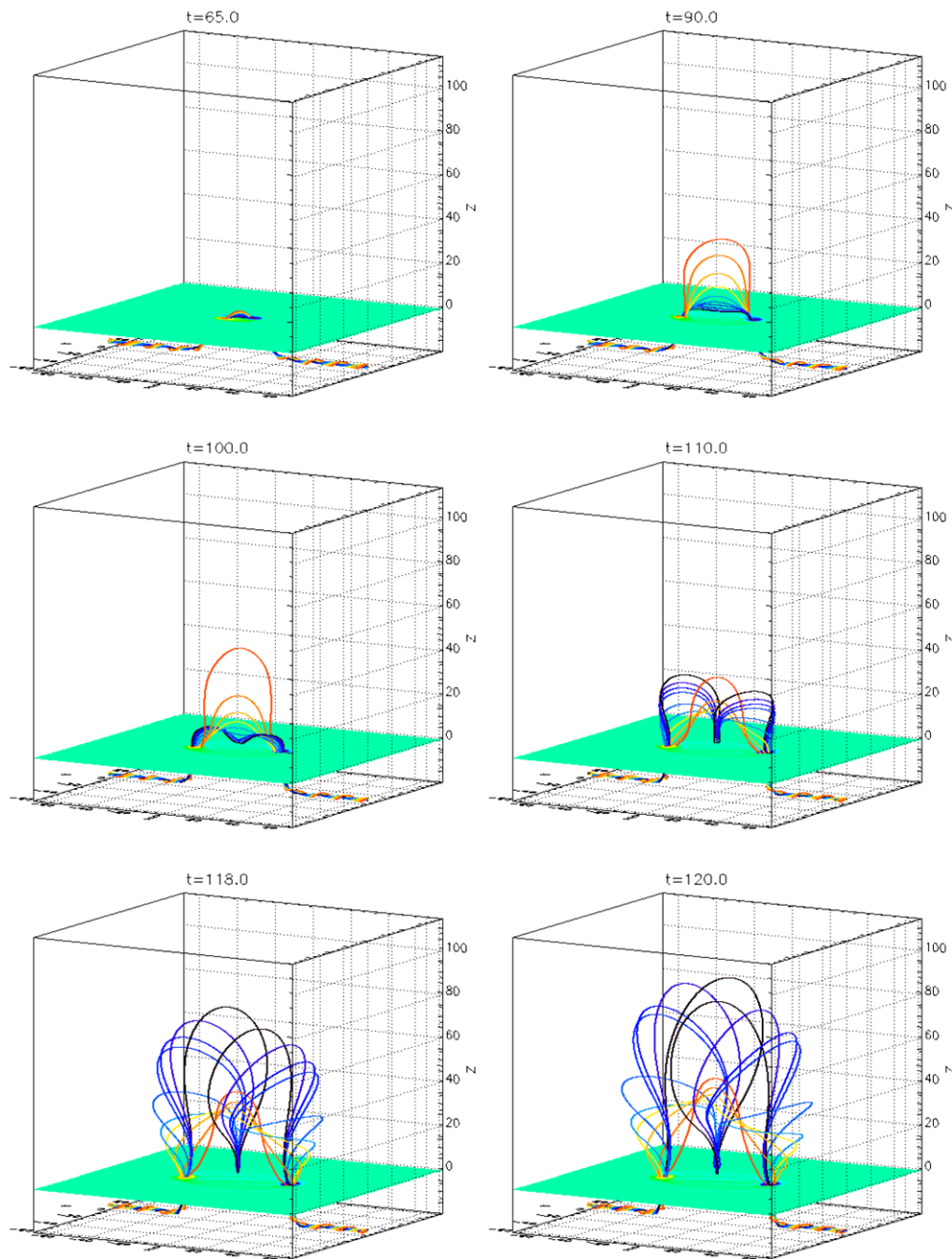


Figure 9. Same as Figure 7, but a different side view perspective.

If we use the specific \mathbf{A} and \mathbf{A}_p given in Equations (17) through (19), it can be shown that the expression, Equation (16), for the relative helicity H_m reduces to simply

$$H_m = \int_{z>0} \mathbf{A} \cdot \mathbf{B} dV. \quad (20)$$

Note that the derivation of the relative magnetic helicity assumed unbounded half space above the photosphere (Berger & Field 1984; DeVore 2000). We carry out the above integral within the simulation domain above $z = 0$ assuming that the field outside of the domain is zero. Thus, our helicity integration only gives an accurate result before the emerged field has expanded to reach the top and side boundaries. It has also been shown (Berger & Field 1984; DeVore 2000) that the rate of change of the relative helicity H_m can alternatively be computed by evaluating the

helicity flux through the $z = 0$ boundary plane:

$$\frac{dH_m}{dt} = -2 \iint [(\mathbf{A}_p \cdot \mathbf{v})\mathbf{B} - (\mathbf{A}_p \cdot \mathbf{B})\mathbf{v}] \cdot \hat{\mathbf{z}} dxdy, \quad (21)$$

where \mathbf{A}_p is given by Equations (18) and (19). The first term on the right-hand side of Equation (21) corresponds to the injection of helicity by horizontal motion on the boundary, and the second term corresponds to injection by direct emergence or submergence of twisted flux across the boundary. Note again, we carry out the above integration on the $z = 0$ plane within the domain, assuming zero flux through the $z = 0$ plane outside of the domain. The resulting evolution of dH_m/dt and H_m for the emerged field above $z = 0$ is shown in Figure 12. In the lower panel of Figure 12, both H_m computed from Equation (16) (solid line) and that obtained by accumulation

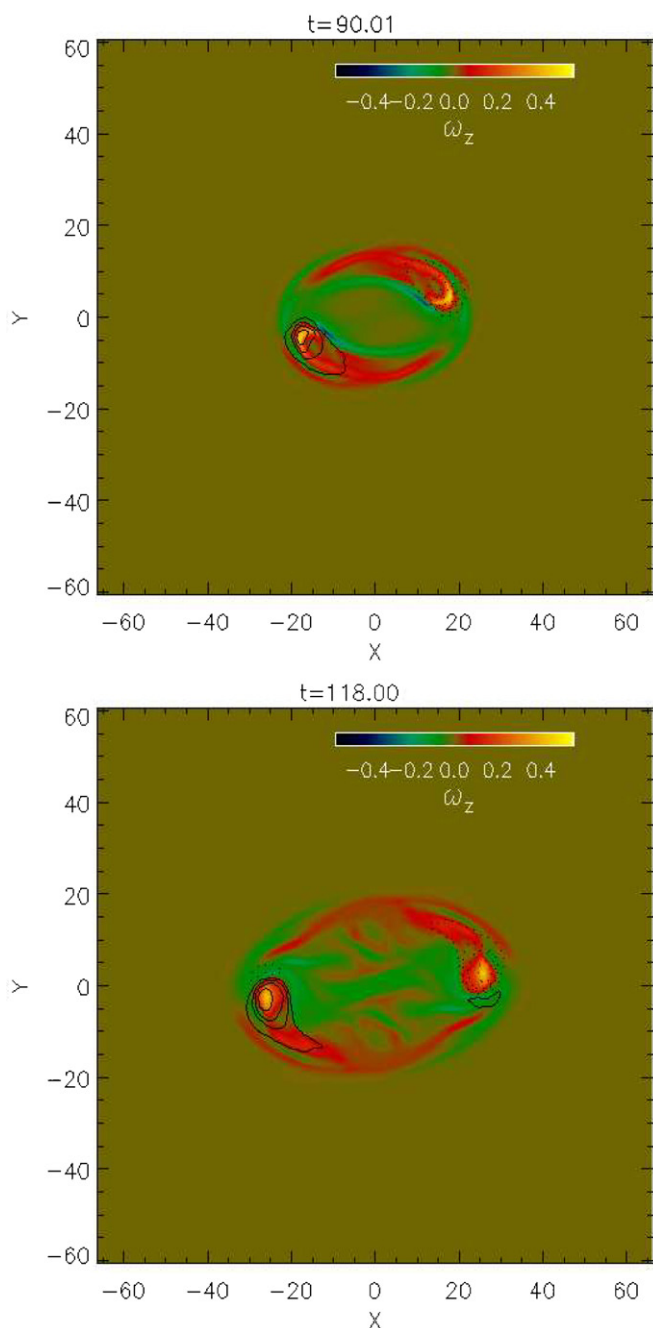


Figure 10. Snapshots of the z -component of the vorticity ω_z on the photosphere overlaid with contours of B_z with solid (dashed) contours representing positive (negative) B_z . The images show counterclockwise vortical motion centered on the peaks of the vertical flux concentration of both polarities.

of helicity flux with time $H_m = \int (dH_m/dt) dt$ (dash-dotted line) are shown. The good agreement of the two indicates good helicity conservation from our simulation. The deviation in the end is due to the fact that twisted magnetic flux is exiting the top and side boundaries and is therefore not accounted for in the integration of Equation (16), while the time integration of dH_m/dt continues to give accurately the amount of helicity that has been transported into the atmosphere through the boundary at $z = 0$. The top panel of Figure 12 shows that the helicity flux due to flux emergence is dominating for a brief period at the beginning (from about $t = 55$ to $t = 80$), and then after about $t = 80$, horizontal shearing and rotational motions at the footpoints of the emerged field become the main source of

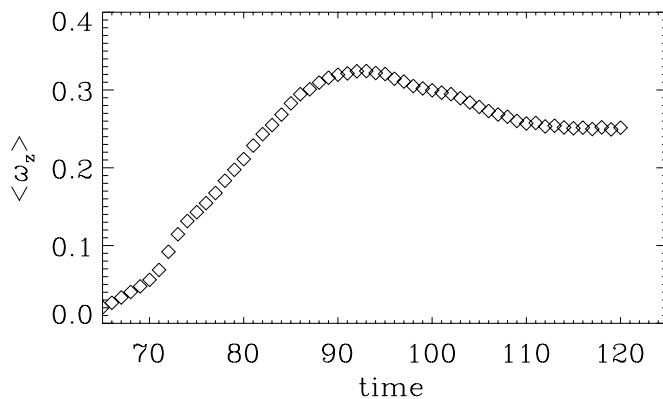


Figure 11. Evolution of the mean vertical vorticity $\langle \omega_z \rangle$ averaged over the area of each polarity flux concentration where B_z is above 75% of the peak B_z value.

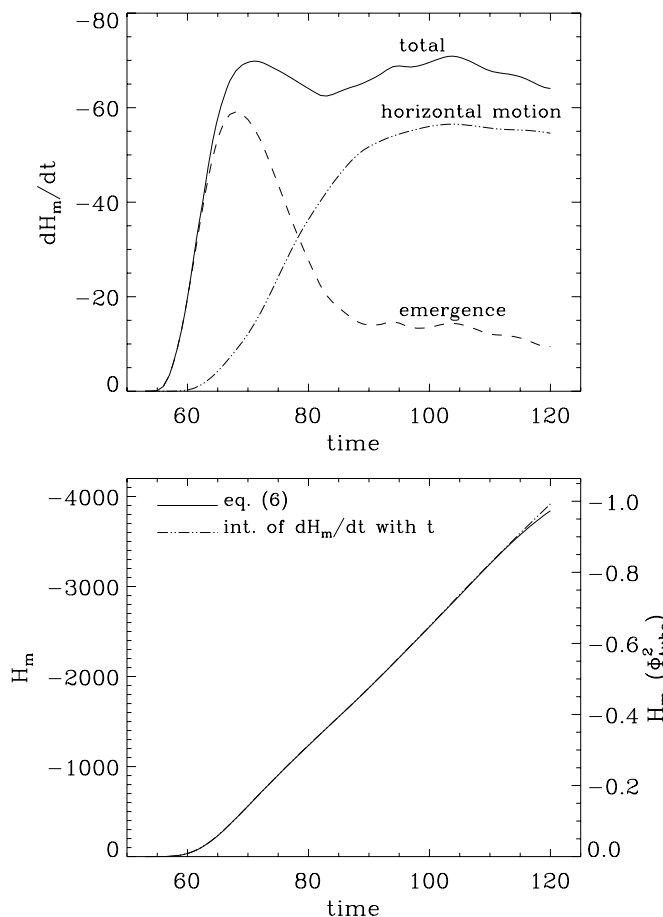


Figure 12. Top panel shows the helicity injection into the atmosphere dH_m/dt due to horizontal motions on the photosphere (dash-dotted line), vertical emergence of flux (dashed line), and the sum of the two (solid line). The bottom panel shows the evolution of the relative magnetic helicity H_m of the emerged field computed from Equation (16) (solid line) and through time integration of the total dH_m/dt (dash-dotted line).

helicity flux. By time of about $t = 90$, the rotational motions in the two polarity flux concentrations have been established (see Figure 11) and they provide a steady and dominant helicity flux into the atmosphere in the subsequent evolution (the top panel of Figure 12). By time $t = 120$, the helicity transported into the atmosphere has reached about $-\Phi_{\text{tube}}^2$, corresponding to one full twist (2π rotation) of the flux Φ_{tube} in the original flux tube.

The rotational motions centered on the two polarity flux concentrations are a manifestation of nonlinear torsional Alfvén

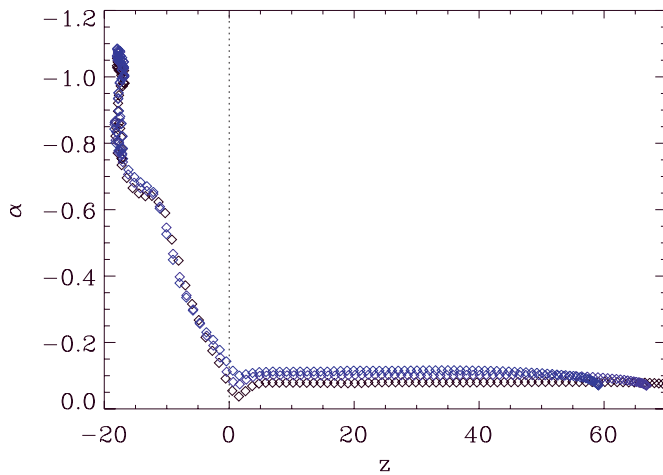


Figure 13. Variation of $\alpha \equiv (\nabla \times \mathbf{B}) \cdot \mathbf{B}/B^2$ as a function of z along three field lines: the black field line shown in Figures 7–9, which is the original tube axis, and its two neighboring blue field lines shown in Figures 7–9, at time $t = 118$. The α values are plotted along these three field lines (using the same colors for the data points as those of the corresponding field lines in Figures 7–9) as a function of depth, from their left ends to the left apices in the atmosphere.

waves propagating along the flux tube, transporting twist from the tube’s interior portion toward its expanded coronal portion. Consider the quantity $\alpha \equiv (\nabla \times \mathbf{B}) \cdot \mathbf{B}/B^2$, which gives a measure of the local rate of twist of the magnetic field. For a force-free magnetic field

$$\nabla \times \mathbf{B} = \alpha \mathbf{B}, \quad (22)$$

from which one can show that

$$\mathbf{B} \cdot \nabla \alpha = 0, \quad (23)$$

i.e., α is constant along each field line for a field with zero Lorentz force. If there is a gradient of α along a field line, then the *thin* flux bundle (or tube) centered on the field line will experience a net axial torque which drives torsional motion of the flux tube (Longcope & Klapper 1997). The net axial torque exerted on a thin flux tube segment $(l, l+dl)$, where l denotes the arc length along the thin tube, is given by Longcope & Welsch (2000, Equation (20) in that paper):

$$\tau_l = \frac{1}{16} a^4 B_l^2 \frac{\partial \alpha}{\partial l} dl, \quad (24)$$

where τ_l represents a torque along the axial direction $\hat{\mathbf{l}}$, which will drive the tube segment to spin about its axis, a denotes the radius of the tube, and B_l denotes the axial field strength. Equation (24) states that the net axial torque τ_l for a thin flux tube segment is directly proportional to the gradient of α along the tube. Note that in Longcope & Welsch (2000) the quantity q , defined as the angle of field-line rotation about the central axis per unit length along the tube, is used in place of α to describe the twist. For a thin flux tube, the relation between α and q is $\alpha = 2q$ (Longcope & Klapper 1997). Figure 13 shows the variation of α along three field lines: the black field line shown in Figures 7–9, corresponding to the original tube axis, and its two neighboring blue field lines shown in Figures 7–9, at $t = 118$. We have plotted the α values along these three field lines (using the same colors for the data points as those of the corresponding field lines in Figures 7–9) as a function of depth, from their left ends to the left apices in the atmosphere, at $t = 118$. We can see that for all three neighboring field lines,

the magnitude of α decreases with height from the interior into the atmosphere. The α is nearly constant along the atmosphere/corona portions of the field lines, indicating that they are near a force-free state, and the coronal value is about a factor of 10 less than the peak magnitude of α in the interior part of the flux tube. The low α magnitude in the corona is due to the extreme expansion and stretching of the magnetic field lines resulting from flux emergence (Longcope & Welsch 2000). The lowered magnitude of α in the atmosphere establishes a gradient of α along the flux tube from the interior to the atmosphere, and produces a torque that drives the observed torsional motion of the flux tube intersecting the photosphere. The torsional motion will continue until the gradient of α along the tube is removed, and the coronal α equilibrates with the interior α (Longcope & Welsch 2000).

3.3. Sigmoid Fields and Current Sheet

The final three-dimensional magnetic field in the atmosphere and corona obtained from the simulation show a coronal flux rope structure whose properties may qualitatively explain some basic observed features of sigmoid active regions. Similar to what was found in Manchester et al. (2004) and Magara (2004, 2006), a current sheet has formed in the lower atmosphere. The top panel of Figure 14 shows the current density J in a horizontal plane at height $z = 10$ in the chromosphere. It shows a horizontal cross section of the current sheet. The current sheet has an overall inverse S shape (except the central zigzag). Field lines traced through a few points along the current concentration on $z = 10$ are also plotted (for different perspectives) in the two lower panels of Figure 14. We find that all the field lines going through the current sheet show an inverse S shape when viewed from the top (as illustrated in the lower right panel of Figure 14), similar to what has been found in the simulations of Magara (2004, 2006) and consistent with the theoretical prediction of Titov & Demoulin (1999) and Low & Berger (2003). One can argue that the heating associated with the current sheet may cause these inverse S shaped field lines to preferentially brighten up in soft X-ray, giving rise to the observed X-ray sigmoid loops in an active region. It can also be seen that some of the field lines undergo sharp dips at the center portion of the current sheet (see the red field lines in the lower left panel of Figure 14). Reconstructions in the current sheet are disengaging the heavy mass trapped in the dips, allowing for the flux rope to rise further into the corona with increasing speed.

We find that the inverse S shaped current sheet begins to develop at the time of about $t = 102$, being initially confined to a few pressure scale heights above the photosphere. With time the current sheet extends upward, and by time $t = 120$, it has extended to the base of the corona. Growing reconnections in the current sheet due to the numerical diffusion inherent in the code are expected to aid the upward acceleration of the center of the flux rope seen after about $t = 102$ (Figure 4(b)). However, the ultimate driver of the rise of the flux rope and the development of the current sheet is the continued vortical motions at the footpoints of the emerged field lines, which transport twist and magnetic energy into the atmosphere, causing an excess of the upward Lorentz force that drives the acceleration.

4. DISCUSSIONS

We have presented a three-dimensional MHD simulation of the emergence of a twisted Ω -shaped flux tube from the top layer of the solar interior into the solar atmosphere and the

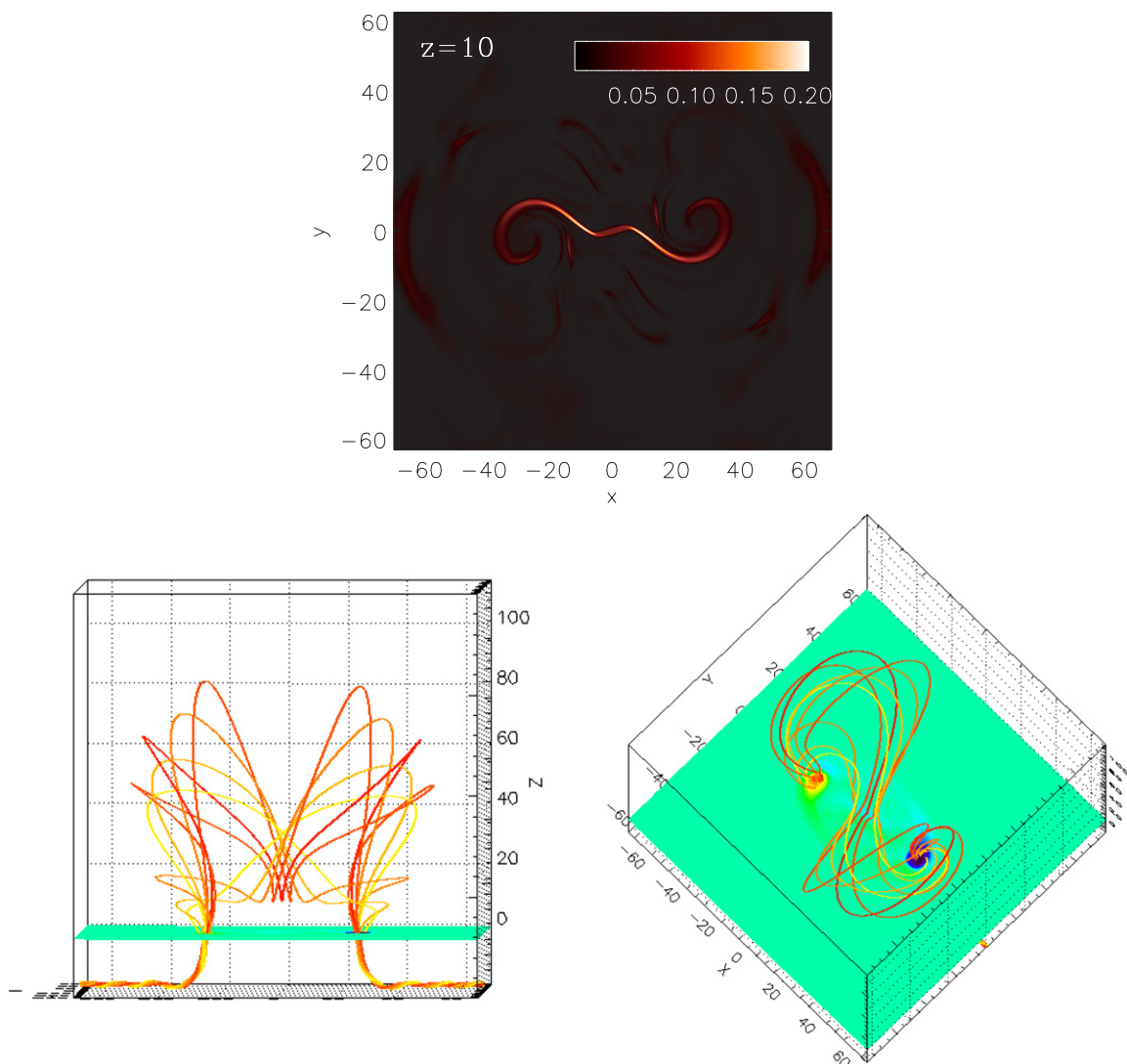


Figure 14. Top panel shows the current density $J = \nabla \times \mathbf{B}$ in a horizontal plane at height $z = 10$ in the chromosphere. The two lower panels show two perspective views of a set of three-dimensional field lines traced from a few points along the current concentration shown in the top panel.

corona. Compared to some of the previous simulations (e.g., Fan 2001; Archontis et al. 2004; Manchester et al. 2004), the subsurface rising flux tube is more sharply arched such that the emerging segment first breaking through the photosphere contains less than one full wind of twist. In this simulation, we find that after an initial stage of flux emergence, during which the two polarity flux concentrations on the photosphere undergo a shearing motion and become separated, a prominent rotational/vortical motion develops within each polarity, reminiscent of sunspot rotations. This rotational motion persists throughout the subsequent evolution and steadily transports twist or magnetic helicity into the atmosphere.

Similar to what has been found in many previous investigations (e.g., Fan 2001; Archontis et al. 2004; Manchester et al. 2004; Magara 2006), the twisted flux tube is unable to rise bodily into the corona as a whole. While the upper parts of the winding field lines of the twisted flux tube expand into the atmosphere and the corona, the center of the original axial field line of the tube ceases to rise at about 2–3 pressure scale heights above the photosphere and the U-shaped parts of the helical field lines largely remain anchored at and below the photospheric layer. However, we find that the initial shearing and the subsequent rotational motions of the two polarity flux concentrations twist

up the inner field lines (near and include the original tube axis) of the emerged field, causing them to rotate in the atmosphere from their initial normal configuration (having a positive B_y at the mid point, or arching over the polarity inversion line from the positive to the negative polarity), into an inverse configuration (having a negative B_y at the mid point, directed from the negative polarity to the positive polarity over the neutral line). This change of the horizontal orientations of the emerged field lines causes an upward propagation of the O-point (the zero-crossing point of B_y , along the center vertical line of $x = 0$ and $y = 0$) in the emerged field in the central vertical cross section ($x = 0$). With the continued twisting of the emerged field lines by the vortical motions at the footpoints, which transports twist and magnetic energy into the corona, the actual plasma motion measured at the O-point also starts to accelerate upward. Thus, the rapid ascent of the O-point is a combination of the upward propagation produced by the change of the horizontal orientations of the field lines and the actual rise of the field lines. As a result, a coronal flux rope with an axial field line identified with the field line instantaneously aligned with the x -direction at its midpoint (i.e., going through the O-point), and with sigmoid-shaped field lines threading under the axis with an inverse configuration, is formed and rises with increasing speed as the vortical motions at

the footpoints continue. Some of the sigmoid-shaped field lines threading under the axis have also develop sharp dips as they are being twisted at the footpoints, with plasma draining into the dips and with the two side lobes rising rapidly into the corona. A current sheet forms in the lower atmosphere with field lines going through it all showing sigmoid shapes. Heating in the current sheet may therefore cause these field lines to brighten up in X-ray as the observed sigmoid loops in active regions. Field lines going through the center portion of the current sheet undergo sharp dips. Reconnections in the current sheet allow for removal of the heavy plasma trapped in the dips and hence enhance the upward acceleration of the coronal flux rope.

The formation of a coronal flux rope with sigmoid-shaped core fields and with a current sheet in the lower atmosphere as a result of the emergence of a twisted flux tube from the interior into the solar atmosphere has been found to be a very general result (e.g., Manchester et al. 2004; Magara 2004, 2006; Archontis & Toëroëk 2008). The onset of a rotational/vortical motion centered on the two polarity flux concentrations soon after they become separated has also been found in Magara (2006). Our work explicitly demonstrates how the vortical motions of the footpoints twist up the inner emerged field lines and rotate them into an inverse configuration (Figures 7–9), leading to the development and upward ascent of the coronal flux rope structure. We also show that the rotational motions of the two polarity flux concentrations on the photosphere are a manifestation of nonlinear torsional Alfvén waves propagating along the flux tube, consistent with what has been predicted by an idealized analytical model of Longcope & Welsch (2000). Due to the rapid stretching of the emerged magnetic field in the atmosphere and corona, the magnitude of $\alpha = \mathbf{J} \cdot \mathbf{B}/B^2$ along the coronal field lines, which is a measure of the rate of twist per unit length, drastically decreases. As a result, a gradient of the rate of twist is established along the flux tube from the interior into the atmosphere with the interior portion of the flux tube having a much higher rate of twist. This gradient in the rate of twist drives torsional waves along the flux tube, transporting twist from the interior highly twisted portion into the expanded coronal portion (Longcope & Welsch 2000). Thus, the rotational motion will continue until the coronal α equilibrates with the interior α along the field lines. The timescale for establishing the equilibrium is on the order of the Alfvén transient time along the interior flux tube, which means that the rotational motion can persist for a few days after the initial emergence. Depending on how great the stretching of the emerged field lines is compared to the total length of the interior flux tube, it is conceivable that the final equilibrated α value is of a significantly smaller magnitude compared to the initial α of the subsurface flux tube rising to the photosphere. This may provide an explanation for the significantly lower α values measured for the majority of the solar active regions compared to the twist rate needed for a buoyant flux tube to rise cohesively in the solar interior.

Sunspot rotations have been observed in many events preceding X-ray sigmoid brightening and the onset of eruptive flares (e.g., Brown et al. 2003; Zhang et al. 2008). Our results suggest that these rotational motions are due to nonlinear torsional Alfvén waves naturally occurring during the emergence of a twisted flux tube, and is an important means whereby twist is transported from the interior into the corona, driving the development of a coronal flux rope as a precursor structure for solar eruptions. The horizontal vortical motion and its subsurface extension corresponding to the torsional Alfvén waves may be detectable by local helioseismology techniques.

I thank B. C. Low and an anonymous referee for helpful comments on the manuscript. NCAR is sponsored by the National Science Foundation. This work is also supported in part by the NASA Heliophysics Guest Investigator Grant NNG07EK66I. The numerical simulations have been carried out on the SGI ALTIX system and IBM POWER5+ system at NASA Advanced Supercomputing Division under project GID s0869, and also on NCAR's IBM POWER6 system.

REFERENCES

- Acheson, D. J. 1979, *Sol. Phys.*, **62**, 23
 Archontis, V., Moreno Insertis, F., Galsgaard, K., Hood, A., & O'Shea, E. 2004, *ApJ*, **426**, 1047
 Archontis, V., & Toëroëk, T. 2008, *A&A*, **492**, L35
 Berger, M. A., & Field, G. B. 1984, *J. Fluid Mech.*, **147**, 133
 Brown, D. S., Nightingale, R. W., Alexander, D., Schrijver, C. J., Metcalf, T. R., Shine, R. A., Title, A. M., & Wolfson, C. J. 2003, *Sol. Phys.*, **216**, 79
 Devore, R. C. 2000, *ApJ*, **539**, 944
 Fan, Y. 2001, *ApJ*, **554**, L111
 Finn, J., & Antonsen, T. M. 1985, Comment. Plasma Phys. Control. Fusion, **26**, 111
 Linton, M. G., Longcope, D. W., & Fisher, G. H. 1996, *ApJ*, **469**, 954
 Longcope, D. W., & Klapper, I. 1997, *ApJ*, **488**, 443
 Longcope, D. W., & Welsch, B. T. 2000, *ApJ*, **545**, 1089
 Low, B. C., & Berger, M. 2003, *ApJ*, **589**, 644
 Magara, T. 2004, *ApJ*, **605**, 480
 Magara, T. 2006, *ApJ*, **653**, 1499
 Magara, T., & Longcope, D. W. 2001, *ApJ*, **559**, L55
 Magara, T., & Longcope, D. W. 2003, *ApJ*, **586**, 630
 Manchester, W., IV. 2001, *ApJ*, **547**, 503
 Manchester, W., IV, Gombosi, T., DeZeeuw, D., & Fan, Y. 2004, *ApJ*, **610**, 588
 Manchester, W., & Low, B. C. 2000, *Phys. Plasmas*, **7**, 1263
 Murray, M. J., Hood, A. W., Moreno Insertis, F., Galsgaard, K., & Archontis, V. 2006, *ApJ*, **460**, 909
 Newcomb, W. 1961, *Phys. Fluids*, **4**, 391
 Rempel, M., Schüssler, M., & Knölker, M. 2009, *ApJ*, **691**, 640
 Shibata, K., Tajima, T., Matsumoto, R., Horiuchi, T., Hanawa, T., Rosner, R., & Uchida, Y. 1989, *ApJ*, **338**, 471
 Stone, J. M., & Norman, M. L. 1992a, *ApJS*, **80**, 753
 Stone, J. M., & Norman, M. L. 1992b, *ApJS*, **80**, 791
 Titov, V. S., & Demoulin, P. 1999, *A&A*, **351**, 707
 Thomas, J. H., & Nye, A. H. 1975, *Phys. Fluids*, **18**, 490
 Zhang, Y., Liu, J., & Zhang, H. 2008, *Sol. Phys.*, **247**, 39